Available online at www.sciencedirect.com
ScienceDirect
Journal of Sound and Vibration 314 (2008) 19–38
JOURNAL OF SOUND AND VIBRATION
www.elsevier.com/locate/jsvi

Control of flexible rotor systems with active magnetic bearings

Shuliang Lei[a,*], Alan Palazzolo[b]

[a]Texas A&M University at NASA Glenn Research Center, MS 301-5, Cleveland, OH 44135, USA
[b]Department of Mechanical Engineering, Texas A&M University, College Station, TX 77843, USA

Received 14 December 2006; received in revised form 10 December 2007; accepted 17 December 2007
Handling Editor: Bolton
Available online 7 February 2008

Abstract

An approach is presented for the analysis and design of magnetic suspension systems with large flexible rotordynamics models including dynamics, control, and simulation. The objective is to formulate and synthesize a large-order, flexible shaft rotordynamics model for a flywheel supported with magnetic bearings. A finite element model of the rotor system is assembled and then employed to develop a magnetic suspension compensator to provide good reliability and disturbance rejection. Stable operation over the complete speed range and optimization of the closed-loop rotordynamic properties are obtained via synthesis of eigenvalue analysis, Campbell plots, waterfall plots, and mode shapes. The large order of the rotor model and high spin speed of the rotor present a challenge for magnetic suspension control. A flywheel system is studied as an example for realizing a physical controller that provides stable rotor suspension and good disturbance rejection in all operating states. The baseline flywheel system control is determined from extensive rotordynamics synthesis and analysis for rotor critical speeds, mode shapes, frequency responses, and time responses.

1. Introduction

Magnetic bearings provide a novel, efficient and effective means for levitating and stabilizing high-speed rotordynamic systems in many applications. In recent years, magnetic bearing technology has found wide applications in both military and commercial machinery [1]. The capability of reacting to applied loads, such as inertia, maneuver or imbalance, as well as the adaptability to changing operating conditions in a wide range of environments derives significant benefits as compared with rolling element bearings. Flywheel systems with magnetic suspensions for energy storage are being utilized in bus, train, and combat vehicles and are being considered in aircraft and space applications. Some advanced magnetic bearing technologies must be developed to be viable for industrial applications of flywheel energy storage systems. The main issues are the stability of the flexible shaft under very high rotation speed and good disturbance rejection from zero to nominal operating speeds. These areas are ultimately addressed by controller and shaft synthesis and systematic component selection in the shaft position feedback loop: position sensors, controller, power amplifiers, and electromagnetic actuators. The objective of this research is to formulate and synthesize a

*Corresponding author.
E-mail address: slei26@gmail.com (S. Lei).

0022-460X/$ - see front matter © 2007 Elsevier Ltd. All rights reserved.
doi:10.1016/j.jsv.2007.12.028

large-order, flexible rotordynamics model with magnetic bearings. Finite element models of the rotor systems are built, and then the finite element flexible models are employed to develop magnetic suspension compensators to provide stable operation over the complete speed ranges. Optimization of the closed-loop rotordynamic properties is obtained via synthesis of eigenvalue analysis, Campbell plots, root locus plots, waterfall plots, and mode shapes.

Control of magnetic bearings has been studied in many papers. Early work in Refs. [2,3] utilized linear proportional-integral-derivative controllers. Advanced control strategies such as optimal control [4,5], μ-synthesis control [6], $H\infty$ control [7], and fuzzy logic control [8,9] have also been applied to magnetic bearing applications. Most of the control strategies utilized a point mass or rigid body model to model the shaft. In reality some vibration modes must be included for reliable and safe levitation at very high speed subject to disturbances. Thus it becomes necessary to build a closed-loop system model including a finite element structural model for describing the shaft and rotor flexibility. A finite element structural model was utilized in Ref. [9] to model a flexible shaft with 24 nodes. Whereas Ref. [9] was mainly focused on a fuzzy logic controller to provide the shaking force on an active stall control rig, the present approach provides a systematic method to synthesize and design the control of magnetic suspensions for rotor support and vibration control. We utilize an example of a vehicle with a hybrid power system, hereinafter referred to as the C-Vehicle, to illustrate a systematic synthesis of the rotordynamic systems with magnetic bearings for open- and closed-loop controller development. A complete overview for the synthesis and design of the magnetic suspension controller for large flexible rotor systems is provided.

The critical vibration modes (resonance frequencies, critical speeds) of the rotordynamic system are a major concern in the design of the magnetic suspension controller. Since the rotor has the maximum vibration amplitudes at these frequencies, great care must be taken to predict and monitor the behavior due to resonance. Conventional rotordynamic analysis with passive bearing supports mainly focuses on natural frequencies that are below, or slightly above, the operating speed. This is a natural consideration since during startup operation, the rotor will successively experience all the critical speeds until the operating speed is reached. Usually passive system designers will at most consider only the lowest three modes [10]. This approach is inadequate for the design of the closed-loop magnetic suspension controller for active magnetic bearing supported rotors. For instance, the example flywheel considered herein has an operating speed of 20,000 rev/min. The modes above this spin frequency should also be considered if they reside within the bandwidth of the controller. The rigid body modeling approach is inadequate since neglecting higher modes may lead to the occurrence of unpredicted resonances and instabilities. The finite element method provides a means to model the flexible system with high accuracy. In the example, the C-Vehicle rotor system has a structural model of 548 degree-of-freedom (137 nodes with four degree-of-freedom per node), which yields 1096 structural states expressed in control canonical form. This model facilitates meeting the requirements for complete synthesis of natural modes in the concerned frequency ranges, and the successful development of a robust and efficient controller.

High-performance rotordynamic systems usually have the following features and concerns: (1) very high spin speed, (2) high centrifugal forces, (3) vibration sensitivity, and (4) stability. The main concerns for the rotordynamic study are vibration amplitude attenuation and system stability in the operating range. In the design of magnetic suspension control for rotordynamic systems, the primary objective is to provide robust, stable and reliable levitation for the fast-spinning, flexible shaft over a wide range of operating speeds subject to disturbance inputs. This design effort requires extensive synthesis and analysis of rotordynamics to determine the rotor critical speeds, mode shapes, frequency responses, and sometimes time responses. The first step is to conduct an open-loop study, i.e. for the rotordynamic system with the magnetic bearings and feedback control loop represented as equivalent springs and dampers. This is useful for determining target values for some support characteristics. Some rotordynamic design concerns include critical speed (i.e. the rotational speed at which vibration due to imbalance is at resonance) placement, steady-state imbalance response, and the occurrence of instabilities. The following approaches are usually employed: (1) rotor balancing, (2) resonance speed placement, and (3) stiffness and damping adjustment [10]. Stability and performance properties may be tuned with closed-loop control when utilizing a magnetic bearing suspension. This operation is typically more difficult when employing conventional ball bearings due to structural limitations.

The controller employed in the flywheel systems includes proportional-derivative, or proportional-integral-derivative controller with lead, tracking notch and fixed notch compensation for stabilization and runout/imbalance rejection. Use of a proportional-derivative (or proportional-integral-derivative) controller without additional compensation would lead to power amplifier saturation and flexible (bending) mode instabilities. Proportional-derivative controllers are robust to modest values of mass imbalance and sensor runout until the required coil voltage is excessive. Therefore, controller refinement is needed to reduce the level of control effort, i.e. the power amplifier voltage. A goal is to optimize the system performance subject to disturbance, noise, and imbalance in terms of the eigenproperties, variation of the amplitude spectrum of coil voltage with rotor spin speed, as well as features of the transient responses. A standard controller optimization for imbalance compensation was implemented to reduce the unacceptable high coil voltage due to mass imbalance and sensor runout. The imbalance compensation employs cascaded notch filters to attenuate the controller response to synchronous disturbances and their harmonics. The centers of the notches track the rotor speed or higher harmonic frequencies.

A physical controller is realized to provide stable rotor suspension with good disturbance rejection, for all planned operating states. A multitude of shaft flexible modes must be controlled along with the rigid body modes. All parts in the flywheel assembly were modeled as flexible structural components, which are expressed as inertia, stiffness and damping-gyroscopic matrices. The necessary information for the synthesis also includes the electromagnetic characteristics of the bearings, i.e. coil inductance and resistance, current stiffness and position stiffness of the actuator.

2. Modeling of flexible rotor systems

2.1. Finite element model formulation

The flexible shaft finite element model is constructed in terms of 3-D beam-type elements. The 3-D beam element configuration is illustrated in Fig. 1.

In Fig. 1, the elastic element vector of displacement and rotation assigned to element i can be arranged in the following convention:

$$U_e = [x_i y_i z_i \theta_{xi} \theta_{yi} \theta_{zi} x_{i+1} y_{i+1} z_{i+1} \theta_{x,i+1} \theta_{y,i+1} \theta_{z,i+1}]^{\mathrm{T}}. \tag{1}$$

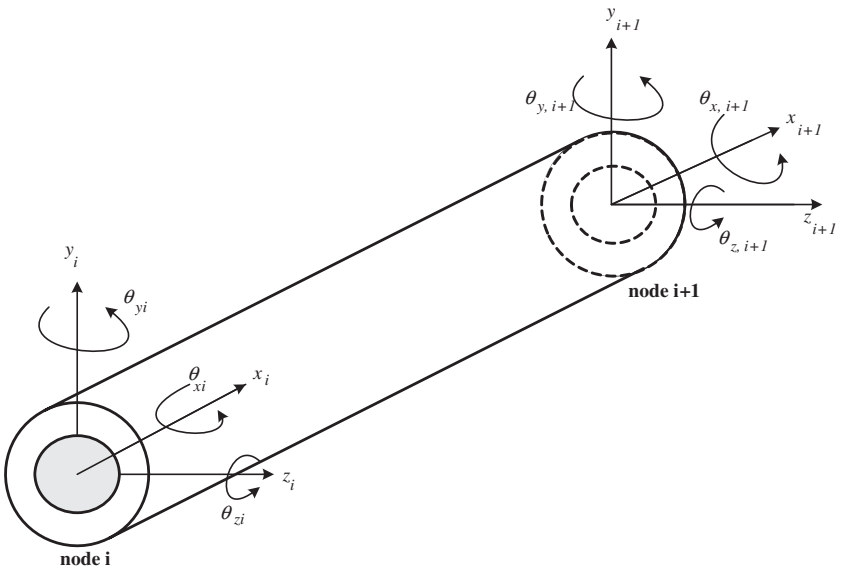

Fig. 1. Three-dimensional beam element for the structural model.

In general, each node in this model has six degree-of-freedom. The main task in formulating a finite element model of a structure is the construction of mass matrix and stiffness matrix. There are two methods to formulate a mass matrix: consistent mass and lumped mass approach. The current approach employs the lumped mass method. The coded finite element algorithms for assembling the mass matrix work equally as well for the consistent mass method. The beam-type finite element stiffness matrix is based on the usual linear elastic assumptions.

In order to obtain a gyroscopic matrix of each element, consider the angular momentum $\mathbf{H} = I_p\boldsymbol{\omega}$ as shown in Fig. 2, where I_p is the element polar moment of inertia, $\boldsymbol{\omega}$ is the angular velocity of the spinning shaft with constant rate ω. Let $\mathbf{i}$, $\mathbf{j}$, $\mathbf{k}$ be unit vectors in the element coordinate. From Fig. 2, we have $\mathbf{H} = I_p\omega\mathbf{i}$. According to Newton's Law, the torque $\mathbf{T}$ applied to the element results in

$$\mathbf{T} = \frac{\mathrm{d}\mathbf{H}}{\mathrm{d}t} = I_p\boldsymbol{\Omega} \times \boldsymbol{\omega}, \tag{2}$$

where $\boldsymbol{\Omega} = \dot{\theta}_x\mathbf{i} + \dot{\theta}_y\mathbf{j} + \dot{\theta}_z\mathbf{k}$ represents the angular velocity of the element coordinate system. The cross product in Eq. (2) gives

$$\mathbf{T} = I_p\omega\dot{\theta}_z\mathbf{j} - I_p\omega\dot{\theta}_y\mathbf{k}. \tag{3}$$

According to the convention in Eq. (1), for node i, we have the gyroscopic matrix as

$$\mathbf{G}_i = \begin{array}{c} \begin{matrix} x_i & y_i & z_i & \theta_{xi} & \theta_{yi} & \theta_{zi} \\ \downarrow & \downarrow & \downarrow & \downarrow & \downarrow & \downarrow \end{matrix} \\ \left[\begin{array}{cccccc} 0 & 0 & 0 & 0 & 0 & 0 \\ 0 & 0 & 0 & 0 & 0 & 0 \\ 0 & 0 & 0 & 0 & 0 & 0 \\ 0 & 0 & 0 & 0 & 0 & 0 \\ 0 & 0 & 0 & 0 & 0 & I_{p,i}\omega \\ 0 & 0 & 0 & 0 & -I_{p,i}\omega & 0 \end{array}\right] \end{array} \begin{array}{l} \leftarrow x_i \\ \leftarrow y_i \\ \leftarrow z_i \\ \leftarrow \theta_{xi} \\ \leftarrow \theta_{yi} \\ \leftarrow \theta_{zi} \end{array} \Big\} \text{Torques.} \tag{4}$$

The external viscous damping is directly added to the related node in the corresponding x_i, y_i, and z_i directions of the $\mathbf{C}$ matrix; that is, the damping coefficients C_{xi}, C_{yi}, and C_{zi} are added to diagonal entries of the $\mathbf{C}$ matrix.

The assembly of the element mass matrix results in a diagonal global mass matrix $\mathbf{M}$ of dimension $6N \times 6N$, where N is the total number of nodes:

$$\mathbf{M} = \mathrm{diag}([m_1 m_1 m_1 I_{p1} I_{t1} I_{t1} \ldots m_i m_i m_i I_{pi} I_{ti} I_{ti} \ldots m_N m_N m_N I_{pN} I_{tN} I_{tN}]). \tag{5}$$

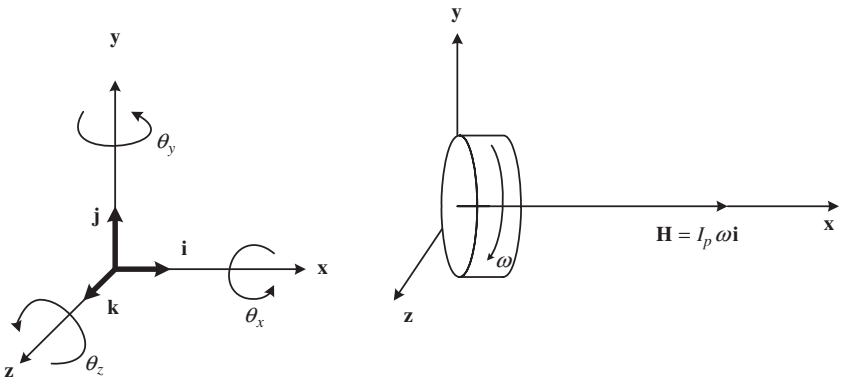

Fig. 2. Coordinate convention and angular momentum vector.

An algorithm and generic code were developed to assemble the element stiffness matrix. Consider the most general case where each node of the element has six degree-of-freedom: displacement in the X, Y, and Z axes and rotation about the X, Y, and Z axes. That is, the element stiffness is formed of a 12×12 matrix. The global stiffness matrix $\mathbf{K}$ is constructed from the element stiffness matrix in terms of the algorithm. Only the radial motion (no torsion or axial) of the shaft is considered in the example; thus, each node possesses four degree-of-freedom.

2.2. C-Vehicle flywheel model

This is a state-of-the-art machine with inside-out structure that employs a vacuum housing to support a non-rotating stator and a magnetically supported composite rotor. The unique feature of the system lies in its capability to support heavy loads, reject disturbances at high speed with minimal friction loss and nominal power consumption. The superior system performance and structural complexity present challenges to the design of the magnetic suspension controller. The mass-elastic model for the rotor, stator and housing consists of 137 nodes. Fig. 3 shows the system configuration. The system stiffness matrix, mass matrix, and gyro-damping matrix are of the dimension 548×548. The model is built on a four degree-of-freedom per node assumption.

There are total 137 nodes in the finite element model including the stator nodes 1–71, rotor nodes 72–126, and housing nodes 127–137. The main system parameters are as follows:

(a) The soft spring stiffness of 17,513 N/m (100 lb/in) connected to ground, at the end plates of the stator at nodes 2 and 70.

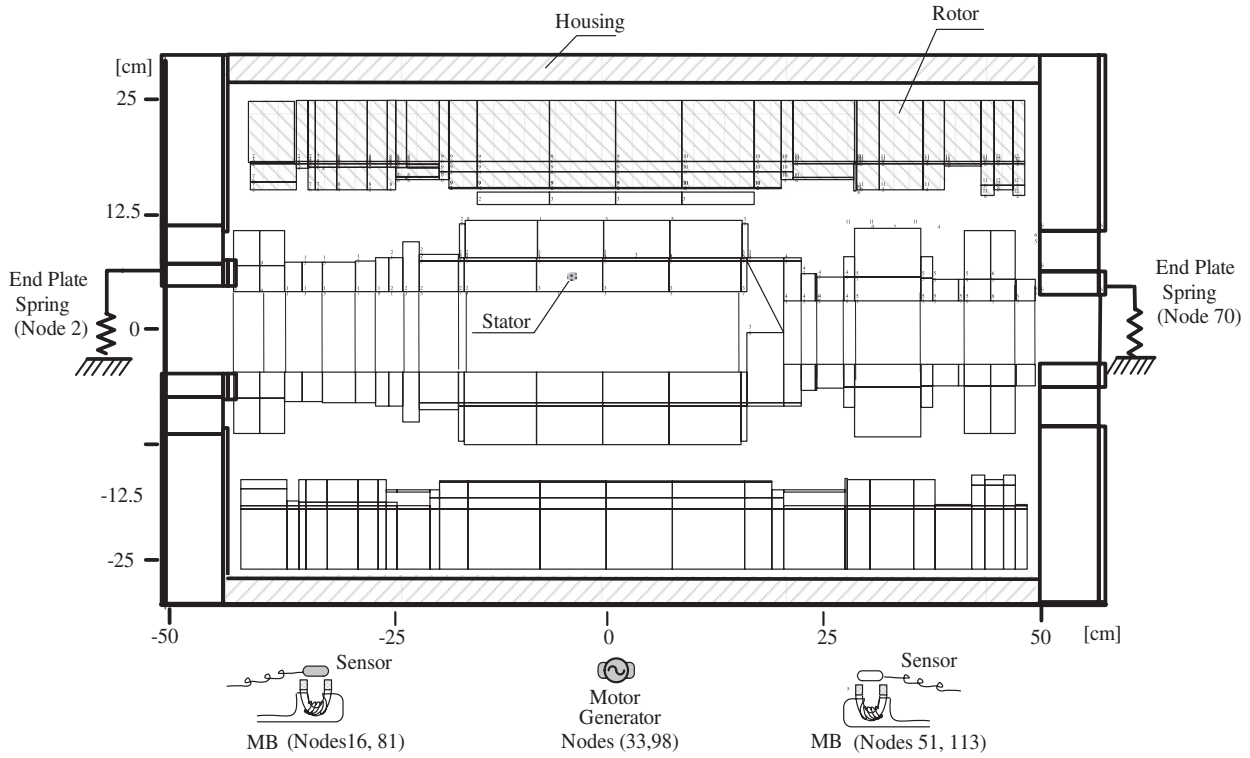

Fig. 3. Configuration of the C-Vehicle flywheel. Finite elements are numbered from the left side, starting with the stator. The three icons at the bottom of the figure indicate the locations of two sensors and a motor generator along the horizontal direction: the sensor on the left side is located at node 16 on the stator connected to node 81 on the rotor; the sensor on the right side is located at node 51 on the stator connected to node 113 on the rotor; the motor generator is located at node 33 on the stator connected to node 98 on the rotor.

(b) The radial magnetic bearings are placed at the stator node 16, which is connected to the rotor node 81, and at the stator node 51, which is connected to rotor node 113.
(c) The motor generator which has a negative stiffness of −875,634.5 N/m (−5000 lb/in) at the stator node 33, which is connected to the rotor node 98.
(d) The current stiffness $K_I = 156.5774$ N/A (35.2 lb/A, per bearing, per axis.

The finite element model was partially verified by comparison with the rigid rotor model by connecting the stator to ground and setting the Young's modulus to an artificially high value. The first four modes for the rigid rotor model are 67, 124, 125, and 274 Hz; modes for the corresponding finite element model are 70, 128, 129, and 274 Hz. The result of the finite element model and that of the rigid rotor model are quite close. Note that the finite element model has a dimension of over 1000, and the dimension of the rigid body model is less than 10. The closeness of the two results provided some confirmation of the correctness of the finite element model.

3. Open-loop rotordynamic system synthesis

The mechanical system of a spinning shaft can be described by the following equation:

$$\mathbf{M}\ddot{\mathbf{U}} + \mathbf{C}\dot{\mathbf{U}} + \mathbf{K}\mathbf{U} = \mathbf{F}_{\text{ext}}, \tag{6}$$

where we assume, for generality, that each node has six degree-of-freedom, and the nodal displacement vector $\mathbf{U}$ takes the following form:

$$\mathbf{U} = [x_1 y_1 z_1 \theta_{x1} \theta_{y1} \theta_{z1} \ldots x_n x_n x_n \theta_{xn} \theta_{yn} \theta_{zn}]^{\mathrm{T}}, \tag{7}$$

where n is the number of nodes.

The $\mathbf{M}$, $\mathbf{K}$, and $\mathbf{C}$ are the mass, stiffness and gyro-damping matrices, respectively, and can be obtained from the finite element method as described previously. In rotordynamics analysis, it is convenient to express the system equation in a first-order ODE expression. To do this, let $\mathbf{Z} = [\dot{\mathbf{U}} \quad \mathbf{U}]^{\mathrm{T}}$, then Eq. (6) becomes

$$\begin{bmatrix} \mathbf{M} & \mathbf{0} \\ \mathbf{0} & \mathbf{I} \end{bmatrix} \begin{bmatrix} \ddot{\mathbf{U}} \\ \dot{\mathbf{U}} \end{bmatrix} + \begin{bmatrix} \mathbf{C} & \mathbf{K} \\ -\mathbf{I} & \mathbf{0} \end{bmatrix} \begin{bmatrix} \dot{\mathbf{U}} \\ \mathbf{U} \end{bmatrix} = \begin{bmatrix} \mathbf{F}_{\text{ext}} \\ \mathbf{0} \end{bmatrix}. \tag{8}$$

That is,

$$\frac{\mathrm{d}}{\mathrm{d}t} \begin{bmatrix} \dot{\mathbf{U}} \\ \mathbf{U} \end{bmatrix} = \begin{bmatrix} -\mathbf{M}^{-1}\mathbf{C} & -\mathbf{M}^{-1}\mathbf{K} \\ \mathbf{I} & \mathbf{0} \end{bmatrix} \begin{bmatrix} \dot{\mathbf{U}} \\ \mathbf{U} \end{bmatrix} + \begin{bmatrix} \mathbf{M}^{-1}\mathbf{F}_{\text{ext}} \\ \mathbf{0} \end{bmatrix}, \tag{9}$$

or, in a more compact form,

$$\dot{\mathbf{Z}} = \mathbf{A}_{\text{mat}}\mathbf{Z} + \mathbf{F}, \tag{10}$$

where

$$\mathbf{Z} = [\dot{x}_1 \dot{y}_1 \dot{z}_1 \dot{\theta}_{x1} \dot{\theta}_{y1} \dot{\theta}_{z1} \ldots \dot{x}_n \dot{y}_n \dot{z}_n \dot{\theta}_{xn} \dot{\theta}_{yn} \dot{\theta}_{zn}, x_1 y_1 y_1 z_1 \theta_{x1} \theta_{y1} \theta_{z1} \ldots x_n y_n z_n \theta_{xn} \theta_{yn} \theta_{zn}]^{\mathrm{T}}, \tag{11}$$

$$\mathbf{A}_{\text{mat}} = \begin{bmatrix} -\mathbf{M}^{-1}\mathbf{C} & -\mathbf{M}^{-1}\mathbf{K} \\ \mathbf{I} & \mathbf{0} \end{bmatrix}, \tag{12}$$

$$\mathbf{F} = \begin{bmatrix} \mathbf{M}^{-1}\mathbf{F}_{\text{ext}} \\ \mathbf{0} \end{bmatrix}. \tag{13}$$

Modal analysis plays an important role in the multidimensional rotordynamic system study. For the multidimensional system of Eq. (12), perform transformation $\mathbf{Z} = \mathbf{T}\boldsymbol{\eta}$ and let $\mathbf{F} = \mathbf{b}\mathbf{u}$, where $\mathbf{u}$ is the input to the system. Eq. (10) changes to

$$\mathbf{T}\dot{\boldsymbol{\eta}} = \mathbf{A}_{\text{mat}}\mathbf{T}\boldsymbol{\eta} + \mathbf{b}\mathbf{u}. \tag{14}$$

Pre-multiply $\mathbf{T}^{-1}$ on both sides:

$$\dot{\boldsymbol{\eta}} = \mathbf{T}^{-1}\mathbf{A}_{\text{mat}}\mathbf{T}\boldsymbol{\eta} + \mathbf{T}^{-1}\mathbf{b}\mathbf{u}. \tag{15}$$

Choosing $\mathbf{T}$ as eigenvector matrix of $\mathbf{A}_{\text{mat}}$, the equation system is diagonalized as

$$\dot{\boldsymbol{\eta}} = \boldsymbol{\Lambda}\boldsymbol{\eta} + \mathbf{T}^{-1}\mathbf{b}\mathbf{u}, \tag{16}$$

where $\boldsymbol{\Lambda} = \mathbf{T}^{-1}\mathbf{A}_{\text{mat}}\mathbf{T} = \text{diag}(\lambda_1, \lambda_2, \ldots, \lambda_n)$ is the eigenvalue matrix with λ_i $(i = 1, 2, \ldots, n)$ as eigenvalues.

For the zero input response, solve the homogeneous equation

$$\dot{\boldsymbol{\eta}}(t) = \boldsymbol{\Lambda}\boldsymbol{\eta}(t). \tag{17}$$

The solution is

$$\boldsymbol{\eta}(t) = \mathrm{e}^{\boldsymbol{\Lambda}t}\boldsymbol{\eta}(0), \tag{18}$$

where $\boldsymbol{\eta}(0) = \mathbf{T}^{-1}\mathbf{Z}(0)$ is the initial condition and

$$\mathrm{e}^{\boldsymbol{\Lambda}t} = \text{diag}([\mathrm{e}^{\lambda_1 t}\mathrm{e}^{\lambda_2 t} \ldots \mathrm{e}^{\lambda_n t}]). \tag{19}$$

Recall that $\boldsymbol{\eta}(t) = \mathbf{T}^{-1}\mathbf{Z}(t)$, we have

$$\mathbf{T}^{-1}\mathbf{Z}(t) = \mathrm{e}^{\boldsymbol{\Lambda}t}\boldsymbol{\eta}(0) = \mathrm{e}^{\boldsymbol{\Lambda}t}\mathbf{T}^{-1}\mathbf{Z}(0). \tag{20}$$

This leads to

$$\mathbf{Z}(t) = \mathbf{T}\mathrm{e}^{\boldsymbol{\Lambda}t}\mathbf{T}^{-1}\mathbf{Z}(0). \tag{21}$$

From control system theory, the zero input response of the original equation $\dot{\mathbf{Z}} = \mathbf{A}_{\text{mat}}\mathbf{Z}$ is

$$\mathbf{Z}(t) = \mathrm{e}^{\mathbf{A}_{\text{mat}}t}\mathbf{Z}(0), \tag{22}$$

where $\mathrm{e}^{\mathbf{A}_{\text{mat}}t}$ can be solved in terms of

$$\mathrm{e}^{\mathbf{A}_{\text{mat}}t} = \mathbf{T}\mathrm{e}^{\boldsymbol{\Lambda}t}\mathbf{T}^{-1}. \tag{23}$$

In fact, the solution of $\mathbf{Z}(t)$ can be drawn from the decoupled system

$$\mathbf{Z}(t) = \mathbf{T}\boldsymbol{\eta}(t) = \mathbf{T}\mathrm{e}^{\boldsymbol{\Lambda}t}\boldsymbol{\eta}(0) = \mathbf{T}\begin{bmatrix} \mathrm{e}^{\lambda_1 t}\eta_1(0) \\ \mathrm{e}^{\lambda_2 t}\eta_2(0) \\ \vdots \\ \mathrm{e}^{\lambda_n t}\eta_n(0) \end{bmatrix} = \begin{bmatrix} \mathbf{T}_1 & \vdots & \mathbf{T}_2 & \vdots & \cdots & \vdots & \mathbf{T}_n \end{bmatrix}\begin{bmatrix} \mathrm{e}^{\lambda_1 t}\eta_1(0) \\ \mathrm{e}^{\lambda_2 t}\eta_2(0) \\ \vdots \\ \mathrm{e}^{\lambda_n t}\eta_n(0) \end{bmatrix}, \tag{24}$$

where $\mathbf{T}_i$, $i = 1,2, \ldots, n$ are the eigenvectors corresponding to the eigenvalues. In structural mechanics, they represent the mode shapes of the corresponding modes associated with the eigenvalues λ_i $(i = 1,2, \ldots, n)$. Hence, we have

$$\mathbf{Z}(t) = \mathbf{T}_1\mathrm{e}^{\lambda_1 t}\eta_1(0) + \mathbf{T}_2\mathrm{e}^{\lambda_2 t}\eta_2(0) + \cdots + \mathbf{T}_n\mathrm{e}^{\lambda_n t}\eta_n(0). \tag{25}$$

Eq. (25) expresses the system output $\mathbf{Z}(t)$ as a summation of eigenvectors $\mathbf{T}_i$ $(i = 1,2, \ldots, n)$ with appropriate vibration mode factors $\mathrm{e}^{\lambda_i t}$, where the natural frequency is the imaginary part of the eigenvalue λ: $\lambda = \varsigma \pm \mathrm{j}\omega$. The eigenvector represents the mode shape; therefore, the solution is expressed in the form of a linear superposition of the modes. Fig. 4 shows that the mode shape (conical mode) of the highest rigid body mode of the rotor and stator components occurs at the frequency 933.9 rad/s = 148.6 Hz = 8918 cpm. Fig. 5 shows that the first bending mode occurs at 3450.5 rad/s = 549.16 Hz = 32,950 cpm.

The first bending mode is well above the operating speed of 20,000 rev/min (333 Hz). The fact that the fundamental flexible mode is far above the maximum operating speed 20,000 rev/min of the machine permits the controller design to ignore the flexible mode, which if present in the actual system can be typically stabilized with a notch filter.

Fig. 6 depicts the C-Vehicle natural frequency map as a Campbell diagram which describes the natural frequency dependence on speed. Note that both the rigid body mode and the first bending mode lie far away

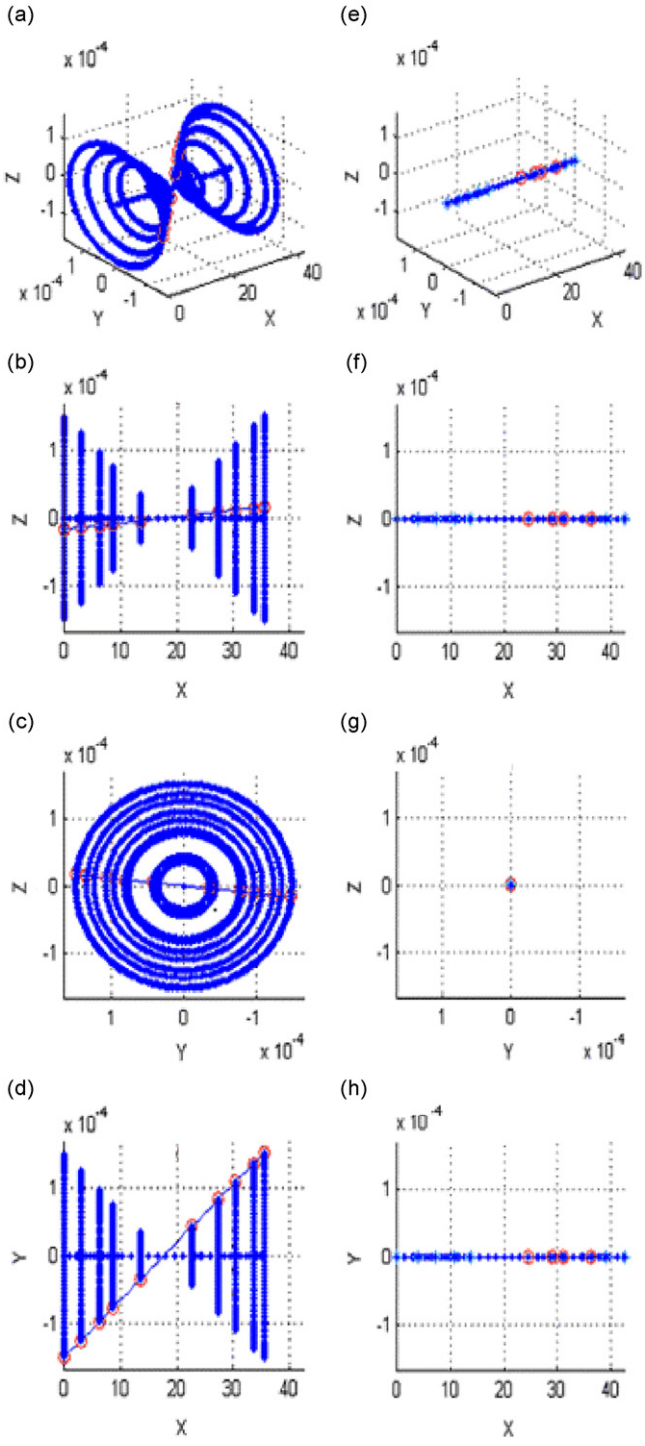

Fig. 4. Conical mode shape of the open-loop C-Vehicle flywheel system. (a)–(d) mode shape of rotor and (e)–(h) mode shape of stator. The red circles are marks for corresponding nodes from different views.

from the operating range as shown in the shaded rectangle. To avoid resonance and interference with the magnetic bearing controller while the flywheel is spinning within its operating speed range, all modes must lie outside this area. All the modes below the highest rigid body mode and above the fundamental flexible mode

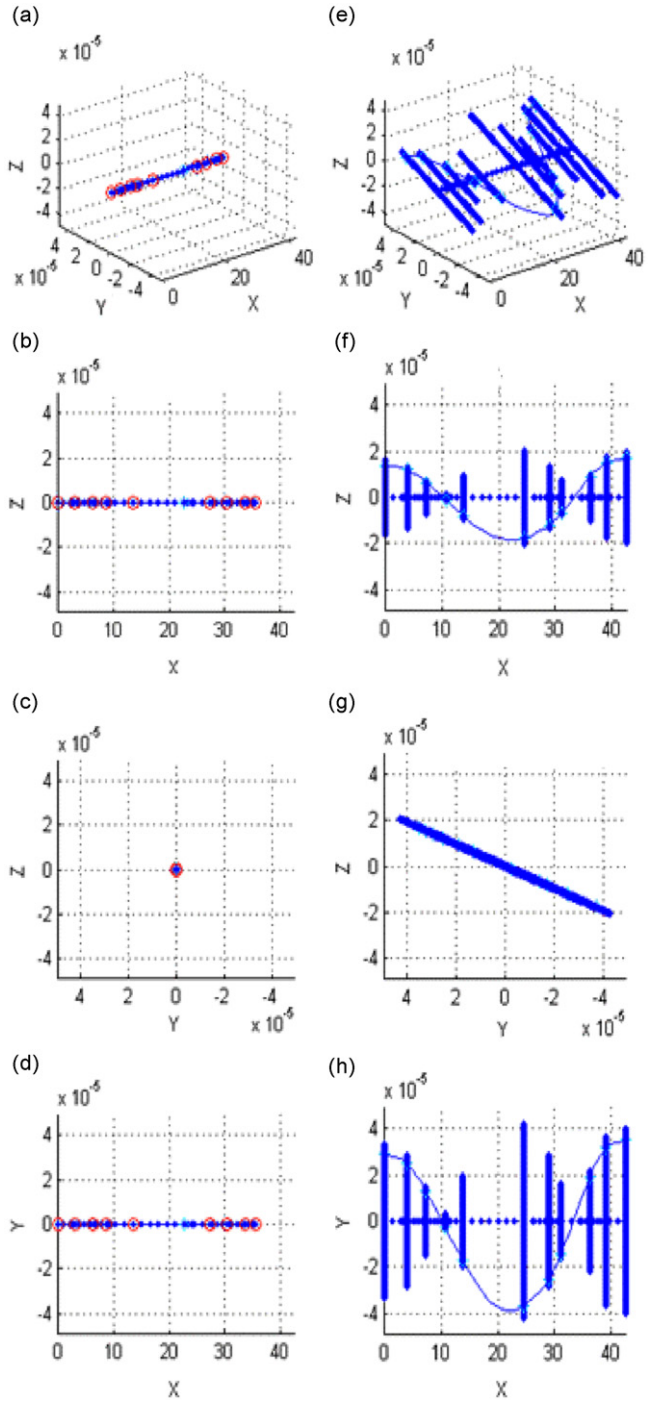

Fig. 5. First bending mode shape of the open-loop C-Vehicle flywheel system: (a)–(d) mode shape of rotor and (e)–(h) mode shape of stator. The red circles are marks for corresponding nodes from different views.

lie in the hatched areas. These two areas do not overlap with the operating speed range. The critical speed is below 5000 rev/min for the complete speed interval 0–20,000 rev/min (the intersection of the operating line with the conical mode is outside the coordinate range of the figure). Actually, as can be seen from the figure, the extension of the operating speed-frequency line (the thick line) and the conical mode line intersects at a

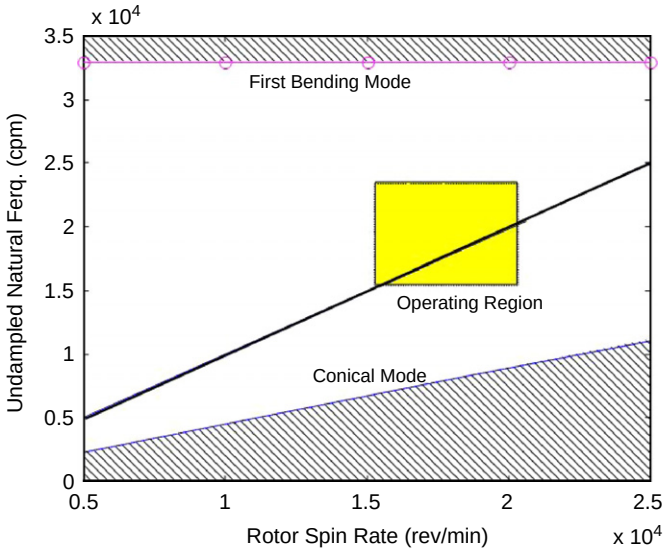

Fig. 6. Campbell plot of the C-Vehicle conical mode and first bending mode.

speed well below 4000 rev/min. Intersections of the operating speed-frequency line (the thick line) with higher modes are well above 25,000 rev/min, which is outside the maximum operating speed range. The first bending mode's natural frequency is speed invariant, whereas the natural frequency of the rigid mode (conical mode) clearly increases with speed.

A conical mode represents a motion with a tilt of the axis of rotation, which forms a conical surface as the axis precesses. This results from the gyroscopic stiffening moment, which becomes stronger as the rotor spins faster. This discussion shows how the open-loop rotordynamic study can aid in designing the magnetic suspension system.

4. Design of magnetic suspension control

Magnetic bearings are active electromechanical suspension systems that apply feedback or feedforward forces as opposed to passive magnetic bearings. In addition to the basic mechanical properties such as stiffness and damping as in passive bearing systems, features unique to the active systems such as rotor positioning, vibration suppression and many others are determined by the controller. In most cases, control is utilized to suspend the rotor in a stable fashion, to suppress vibrations due to imbalance and to reject the disturbance such as those from the sensor runout. The most widely used control is the proportional-integral-derivative control with appropriate filters. The control system allows the current in the bearing coil to be adjusted based on the shaft position sensor signals. This closed-loop control is necessary for the shaft to be held in a stable position. Typically the control system contains path filters, compensators, amplifiers, actuators and in some cases notch filters [11]. The controller commands the power amplifiers to maintain specific time-varying currents; therefore, an inner feedback loop for controlling the current is present in the power amplifier. From a mechanical point of view, a magnetic bearing system behaves similar to a spring–damper system. The magnetic actuator is an open-loop unstable plant; that is, it behaves as a "spring" with negative spring constant. A simple transfer function can describe the "plant" as

$$G(s) = \frac{1}{ms - K_{\mathrm{MB}}}. \tag{26}$$

An ideal proportional-derivative controller $H(s)$ provides the necessary spring and damping capability to the system as

$$H(s) = Cs + K. \tag{27}$$

In many applications, proportional-derivative controllers have been selected for active magnetic bearing controllers [12,13]. This is primarily due to their intuitive appeal: proportional control relates directly to spring stiffness, whereas derivative control relates to bearing damping. In real control implementation, we will not be able to realize the ideal control $H(s) = K+Cs$ since the control dynamics must also be considered. Also, due to the consideration of shaft flexibility and gyroscopic effect, the stability criterion cannot be directly drawn by mere inspection of the signs of the coefficient of the second-order system. However, the above analysis gives a qualitative estimation of control parameters and preliminary design baseline. A necessary condition to stabilize the rigid body mode is to have $K > K_{\mathrm{MB}}$.

In practical digital implementations, proportional-derivative controllers are processed as first- or second-order digital filters with limited cutoff frequency. Bilinear transformations are used to convert the s-domain transfer function into time-domain difference equations. The proportional controller $P(s)$ and the derivative controller $D(s)$ take the forms $P(s) = K_p/(\tau_c s + 1)$ and $D(s) = K_d s/(\tau_c s + 1)^2$, where K_p and K_d are proportional and derivative gain, respectively, τ_c is time constant. If the cutoff frequency $1/2\pi\tau_c$ goes to infinity, we have the ideal case.

The term $\mathbf{F}$ in Eq. (10) represents the magnetic bearing controller forces and disturbances, where the controller forces are generated by the magnetic bearing actuators. The controller forces are included in the closed-loop system matrix of the equation

$$\dot{\mathbf{W}}_{\mathrm{sys}} = \mathbf{A}_{\mathrm{sys}}\mathbf{W}_{\mathrm{sys}} + \mathbf{B}_{\mathrm{sys}}\mathbf{u}_{\mathrm{sys}}, \tag{28}$$

where $\mathbf{W}_{\mathrm{sys}}$ is a system vector that contains structural variables as well as the controller states. $\mathbf{A}_{\mathrm{sys}}$ is a closed-loop system matrix that includes the structural stiffness matrix, the mass matrix, the gyroscopic matrix, the damping matrix, and the controller dynamics. $\mathbf{B}_{\mathrm{sys}}$ is the external input matrix that accounts for the disturbances of imbalance and runout. The system performances can be obtained by the eigenanalysis of the $\mathbf{A}_{\mathrm{sys}}$ matrix. The proportional-derivative controller and compensators used in the flywheel unit analysis and simulation are given as follows:

Proportional control: first-order filter:

$$P_s(s) = \frac{K_p}{\tau s + 1}. \tag{29}$$

Derivative control: second-order filter:

$$D_s(s) = \frac{K_d s}{(\tau s + 1)^2} = \frac{K_d s}{\tau^2 s^2 + 2\tau s + 1}. \tag{30}$$

Lead compensator:

$$L_s(s) = K_{\mathrm{ld}}\frac{s - z_0}{s - p_0}, \tag{31}$$

where K_{ld} is the gain of the lead compensator, the zero and pole are $z_0 < 0$ and $p_0 < 0$, respectively.

The notch filter has the form

$$\frac{y(s)}{x(s)} = \frac{s^2 + \omega_0^2}{s^2 + (\omega_0/Q)s + \omega_0^2}, \tag{32}$$

where ω_0 is the notch center frequency. The parameter Q determines the width of the notch in the frequency response. The larger the Q values, the smaller the width of the notch and the less its effect on the phase lag. Generally, this value is chosen below 30 for practical considerations, and in this design all the Q values are chosen to be 10.

4.1. C-Vehicle closed-loop model

The major components of the C-Vehicle flywheel system consist of the stator, rotor, vacuum vessel and plates (modeled as springs to ground). All parts in the flywheel assembly were modeled as flexible structural components, which are represented as inertia, stiffness and damping-gyroscopic matrices. Required

information for the synthesis also includes the electromagnetic characteristics of the bearings, i.e. coil inductance and resistance, and current stiffness and position stiffness of the actuator. The mass-elastic model for the magnetic bearing rotor, stator and housing consists of 137 nodes. The structural and actuator models were incorporated into a feedback control loop of the entire model consisting of over 1096 structural degrees of freedom plus controller states. The magnetic bearing has a homopolar architecture which provides forces through axial as well as circumferential flux flow. This configuration reduces eddy current and hysteresis losses.

The controller of C-Vehicle flywheel utilizes a linear decentralized controller, which includes a proportional-integral-derivative with lead, tracking notch and fixed notch compensation for stabilization and runout/imbalance rejection. The mathematical model of the closed-loop system of a C-Vehicle flywheel magnetic suspension control is described in Eq. (28). The architecture of the controller is illustrated in Fig. 7. Use of a proportional-integral-derivative (or proportional-derivative) controller without additional compensation would lead to power amplifier saturation and flexible (bending) mode instabilities.

The following steps were employed iteratively to optimize the controller. Step 1 is to tune the proportional-derivative controller gains K_p and K_d in order to obtain stable levitation. This requires that a desired static bearing stiffness be selected to overcome the negative stiffness and maintain stability over a wide range of modes. The challenges this construction presented for magnetic suspension control to include a multitude of shaft (core) flexible modes that must be controlled along with the rigid body translation, nutation and precession modes of the rotor. The second step is to utilize linear stability analysis to identify a proportional-derivative controller for the complete operating speed range. Using selected proportional-derivative gains, simulations are carried out to confirm that the entire speed range 0–20,000 rev/min is stable. Whereas the proportional-derivative controllers are robust to modest values of mass imbalance and sensor runout, the required coil voltage is excessive. Therefore, in the third step, controller refinement is made to reduce the level of control effort, i.e. the power amplifier voltage. The system performance is optimized subject to runout, noise, and mass imbalance forces by inspecting the predicted amplitudes of the harmonic spectrum, waterfall plot, and transient response plots. A controller compensation technique was implemented to reduce the unacceptable high coil voltage due to mass imbalance and sensor runout. The compensation employs cascaded notch filters to attenuate the controller response to synchronous disturbances and their harmonics. The centers of the notches track the rotor speed or higher harmonic frequencies. The fourth step is to design the controller

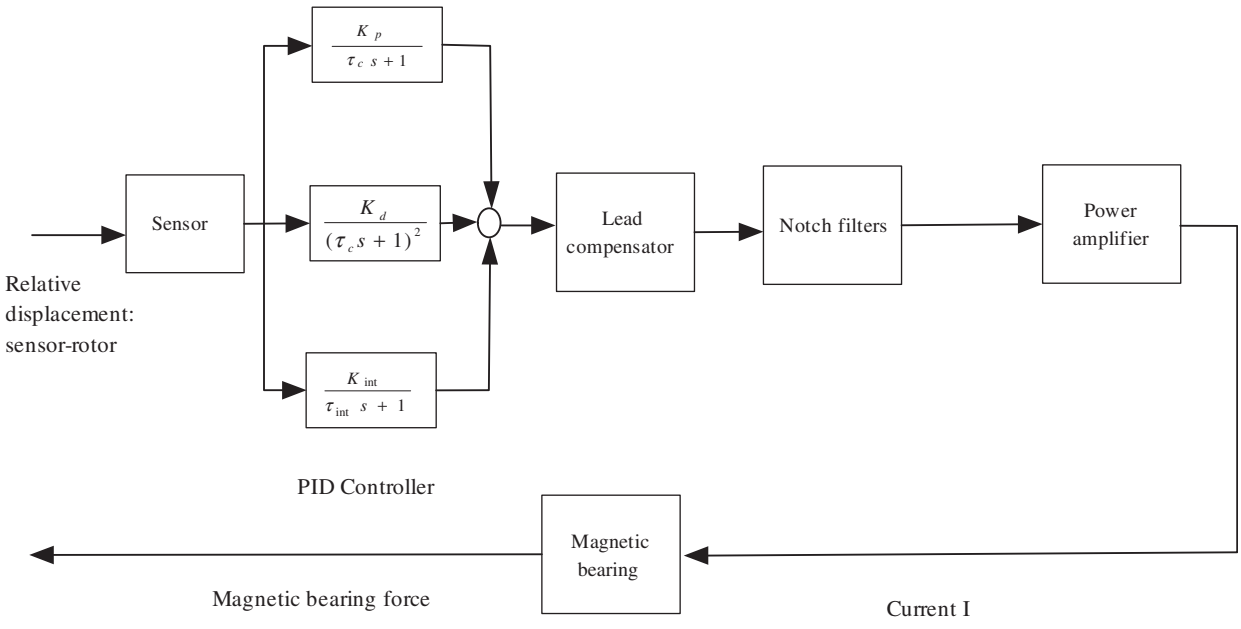

Fig. 7. Control architecture of the C-Vehicle flywheel.

to reject inertial load disturbances due to vehicle maneuvers. An integration stage is added to the controller for this purpose.

4.2. Stability

Stability is the primary concern, among the other specifications due to the energy and speed of the flywheel. The first design step is to choose suitable proportional and derivative gains at the normal operating speed, 20,000 rev/min to ensure stability of all modes in the targeted bandwidth ~1100 Hz. To attain this, an automated, root-locus-like, computer search procedure was carried out for $K_p = 0$–80 and $K_d = 0$–0.05. The stability results were presented as an eigenvalue list: the real part of the eigenvalue represents the damping of the mode; the imaginary part of the eigenvalue is the modal frequency, and a negative real part of the eigenvalue indicates stability at that modal frequency. The closed-loop system included over 1000 structural and control related state variables. The computation results gave the preliminary range of the values for K_p and K_d: $K_p = 5$–15 and $K_d = 0.0001$–0.001. Lead compensators and fixed notch filters were also included in the controller stage cascade to improve the phase property of the closed-loop system. Campbell plots and mode shape plots were also utilized to evaluate the system's stability. With $K_p = 6$ and $K_d = 0.0002$ the corresponding effective magnetic bearing stiffness is $K_{\text{eff}} = K_p G_{\text{sen}} G_{\text{PA}} K_I - |K_{\text{pos}}| = 148{,}256\,(\text{N/M}) = 17{,}977\,(\text{lb/in.})$. The controller cutoff frequency was selected as $f_{\text{ccut}} = 1100$ Hz. This choice reflects the practical consideration that it is difficult to implement controllers with very high-frequency bandwidths due to noise amplification.

The center frequencies of the notch filters are 1X, 10,500 (rad/s), 6X, 11X, 12X, 13X, and 7500 (rad/s). The choice of the notch center frequencies is based on the following synthesis: The tracking notches 1X, 6X, 11X, 12X, and 13X track the synchronous signal (1X) and the higher harmonic signals (6X, 11X, 12X, and 13X) in order to remove the respective harmonic disturbance from the sensor runout. The fixed notches centered at 7500 rad/s (1193 Hz) and 10,500 rad/s (1671 Hz) are used to stabilize the modes adjacent to these frequencies. The lead compensators are then utilized to compensate for the phase lag due to the notch filters to ensure all eigenvalues are located on the left half-plane. Lead compensators have center frequencies of 10,000, 6630, and 7812 rad/s and the corresponding gains are: 18, 4, and 6. The final determination of the controller parameters is based on an exhaustive iterative search. The maximum stable modal frequencies with different operating speeds are given in Table 1.

At low operating speed, the notches have a significant negative impact on the stability of the system. To maintain stability in the entire operating range, the 1X synchronous notch and the fixed notch centered at 7500 rad/s are turned off below 4000 rev/min. The synchronous 1X notch is turned on at 8000 rev/min and the fixed notch is turned on at 16,000 rev/min. This control strategy results from the study of the Campbell plot: a plot that displays the root locus change with rotation speed. In the Campbell plots, the real parts and the imaginary parts are drawn against the rotation speed separately. According to the synthesis, at low rotation speed with all the notches turned on, some of the modes become unstable: the locus of the real parts of the eigenvalues vs. speed crosses the zero line and attains positive (unstable) values. The Campbell plots were drawn from the eigenvalue lists at the associated rotational speeds. In the eigenvalue computations, the notch center frequency appears as a modal frequency in the eigenvalue list. Therefore, it should be noted that, due to the introduction of the notch filters, the eigenvalue list of the closed-loop system includes the notch center frequencies. Figs. 8–10 are the closed-loop Campbell plots of rigid body modes and bending modes, respectively.

Table 1
Variation of the maximum stable modal frequency with speed

Rev/min		4000	8000	12,000	16,000	20,000
Maximum stable modal frequency	(rad/s)	10,912	10,950	10,902	10,901	10,895
	(Hz)	1736	1743	1735	1735	1734

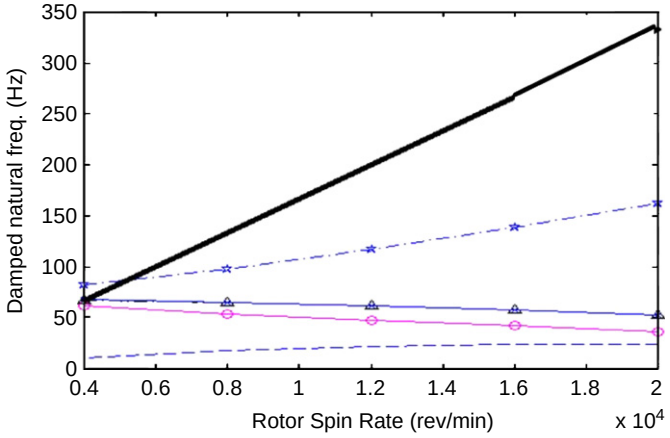

Fig. 8. Closed-loop Campbell plot: damped natural frequency vs. speed for rigid body modes. The solid thick line is operating speed line. The other four curves depict the rigid body modes: first mode: conical mode (– –), second mode: conical mode (○—), third mode: cylindrical mode (△—), and fourth mode: cylindrical mode (☆ —·—).

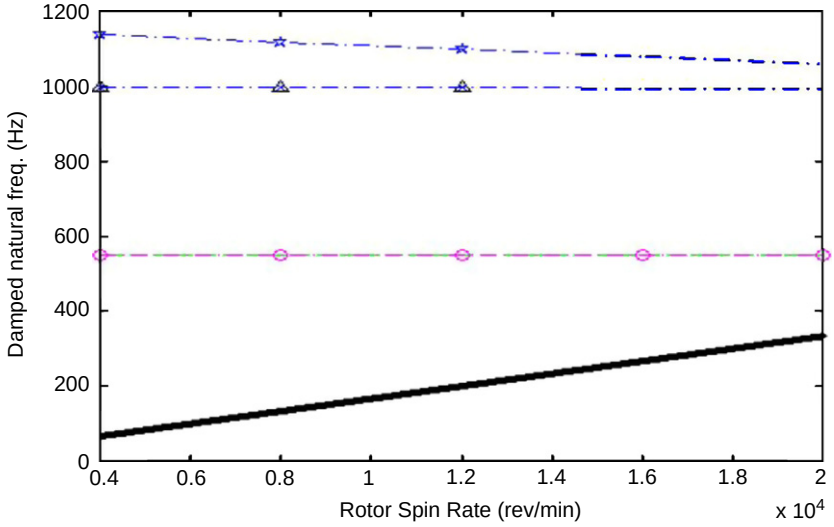

Fig. 9. Closed-loop Campbell plot: damped natural frequency vs. speed for bending modes. The solid thick line is operating speed line. The other three curves are bending modes: first bending mode: (○—·—), second bending mode (△—·—), and third bending mode: (☆ —·—).

Fig. 8 depicts the rigid body modes: the first mode and the second mode are the forward and backward conical mode, respectively, which change with rotation speed due to the gyroscopic effect of the flywheel. The third and the fourth modes are the forward and backward cylindrical modes, respectively. It clearly shows the forward and backward mode splitting with increased speed. The thick black line in Figs. 8–10 represents the operating speed change. The intersection of this line with the modal frequency curve determines a critical speed. At low frequencies, one critical speed occurs at 5000 rev/min, and the other critical speeds lie below 5000 rev/min. These lower critical speeds are away from the normal operating region (refer to open-loop Campbell plot) by a large margin. At higher frequencies, Figs. 9 and 10 show that the critical speeds all lie well above 20,000 rev/min. These critical speeds occur with bending modes. From the Campbell plots, it can be concluded that all modes are stable for the entire speed range. The highest damped natural frequency is over 1700 Hz.

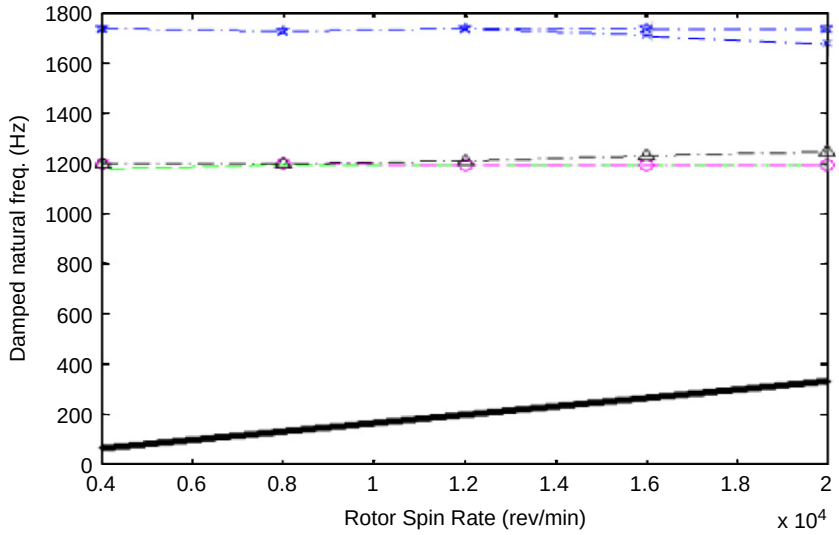

Fig. 10. Closed-loop Campbell plot: damped natural frequency vs. speed for higher bending modes. The solid thick line is the operating speed line. The other four curves are higher bending modes. The bending modes split into forward and backward modes: forward bending mode (○—·—), backward bending mode (△—.—), forward bending mode (*–·–), and backward bending mode (☆—·—).

4.3. Disturbance rejection

There are three main sources of disturbance in the flywheel system: sensor runout, imbalance, and noise. The first two types of disturbances are synchronous to the rotation speed whereas the last one may have random amplitude and frequency range. Synthesis and simulations have shown that the most hazardous disturbance is the runout and imbalance. The multi-harmonic runout causes large increase in the control coil voltage that exceeds the power amplifier limitations. A critical speed is experienced when vibration amplitudes peak at a speed coincident with a modal frequency. These speeds were obtained from a Campbell diagram of the closed-loop damped natural frequencies vs. speed. The results for the C-Vehicle rotor show that the critical speeds are below 5000 rev/min. The forward conical mode creates a critical speed since its I_p/I_t ratio is less than unity. Critical speed vibration is excited by imbalance and the first harmonic of runout. The parameters of the imbalance distribution employed for the C-Vehicle model are: position of imbalance 1 is at node #81; position of imbalance 2 is at node #113; eccentricity of imbalance is $e = 0.635\,\mu\text{M}$; imbalances at both ends have a 90-degree phase difference. The sensor runout has 23 harmonics. The amplitude and phase angle of each harmonics are listed in Table 2.

Notch filters are used to suppress the imbalance and runout disturbances to alleviate the related control effort. A frequency response (Bode plot) of the controller is depicted in Fig. 11.

The function of the notch filters can be obviously seen from the plots of controller frequency responses. The synchronous disturbances of runout and imbalance occurred at the "peak" area of the Bode plot of the controller, which magnifies the disturbances. The introduction of the notches traps the synchronous disturbance signal to alleviate the control effort in the magnetic bearing coil. The phase lag effect of notch filters can be seen at the frequency range below the notch center frequency in the Bode plot. The determination of tracking notch harmonic numbers is based on the control output signal spectrum. The introduction of the notch filters should ensure that the harmonics with high peak values are effectively trapped. A more sophisticated way to determine the harmonic spectrum is a waterfall plot. A waterfall plot is a three-dimensional harmonic spectrum with the rotor spin rate as the additional dimension. In rotordynamics, the waterfall plot depicts the frequency spectrum changes with rotation speed. Fig. 12 is the waterfall plot of the closed-loop system. As depicted in the waterfall plot, at 20,000 rev/min, the main contribution to the control coil voltage comes from harmonics 2, 3, 4, 5, 7, 8, and 9. The first and the

Table 2
The magnitude and phase at the harmonics in the sensor runout data

Harmonics	Magnitude (μM)	Phase (deg)
1	1.168	−233.5
2	0.914	−208
3	0.609	−52
4	0.645	−52.5
5	0.423	−303
6	0.505	−248
7	0.264	−396
8	0.318	−200
9	0.155	−340
10	0.114	−300
11	0.269	−474
12	0.307	−365
13	0.213	−555
14	0.312	−615
15	0.439	−310
16	0.109	−388
17	0.254	−360
18	0.208	−600
19	0.137	−900
20	0.508	−1030
21	0.239	−857
22	0.094	−770
23	0.315	−990

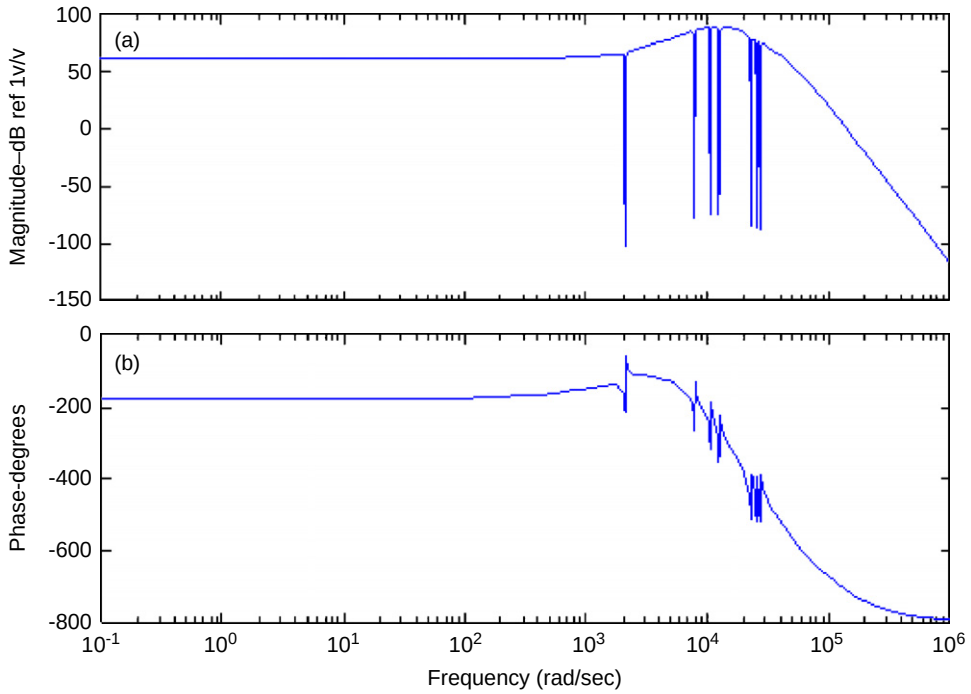

Fig. 11. Magnitude (a) and phase (b) of the frequency response function of the C-Vehicle controller.

sixth harmonics are effectively notched off by the tracking notches. It should be mentioned that before cascading the notches in the controller, the coil voltage is so high that it almost reached 1000 V at normal rotation speed.

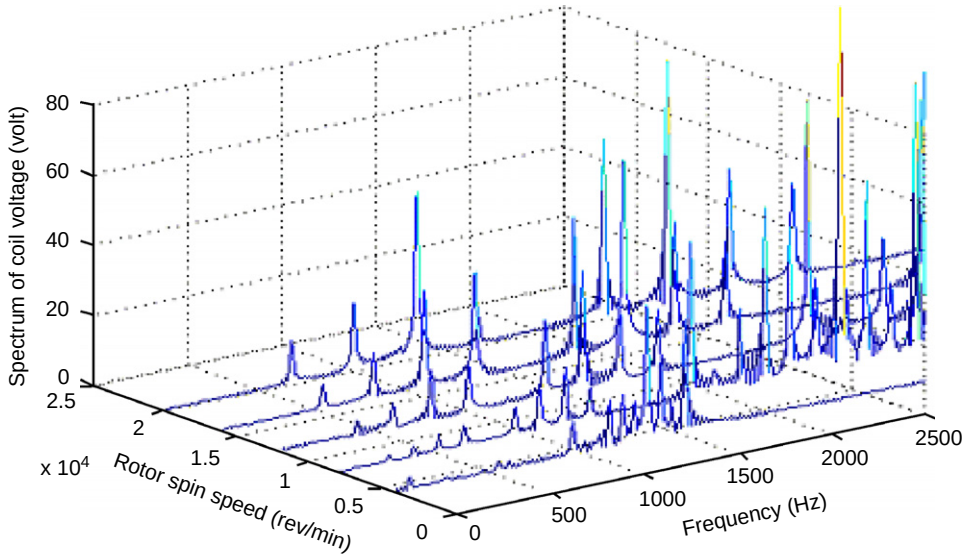

Fig. 12. Variation of the amplitude spectrum of the coil voltage with rotor spin speed.

In the Bode plot of the controller at normal operating speed (Fig. 11), the seven cascaded notches are: 1X (333.33 Hz, 2094.4 rad/s), fixed notch (7500 rad/s), fixed notch (10,500 rad/s), 6X (2000 Hz, 12,566 rad/s), 11X (3666.66 Hz, 23,038 rad/s), 12X (4000 Hz, 25,132 rad/s), 13X (4333.3 Hz, 27,227 rad/s).

In Table 2, the experimental runout data decomposed the signal into harmonics of different amplitudes (in μM) and phase angles (in degrees). The resulting data showed that the first harmonic runout amplitude is 1.168 μM, the highest one among the total 23 runout harmonics. However, since this frequency falls into the flat area of the frequency response, the resulting output due to this harmonic is not very large. After the 13X harmonics (27,227 rad/s), the Bode plot shows that the amplitude of the frequency response is decreasing steeply.

4.4. Transient simulations and response to inertial load

Transient simulations showed that the flywheel system was well stabilized. Time responses of the motions of the magnetic bearings are bounded well within the air gap subject to all the disturbances. The coil voltage outputs with imbalance and sensor runout at 20,000 rev/min are displayed in Fig. 13.

As the vehicle is maneuvering, the flywheel is subject to inertial loading, which in turn loads the magnetic suspension system. For example, if the vehicle experienced a sudden step g-load, the rotor would have a steady-state error (position offset) in a proportional-derivative control system without an integrator. This offset is undesirable because a big steady-state offset may cause the rotor to hit the stator and fail the magnetic suspension. Integration control assures accurate position and alignment of the rotor. For the convenience of implementations, a first-order low pass filter with very low cutoff frequency is used to approximate an integrator:

$$\frac{K_{\text{int}}}{\tau_{\text{int}} s + 1}, \tag{33}$$

where the time constant τ_{int} can be set in the range of 10–100 s.

The effect of the time constant τ_{int} is tested via simulations with the C-Vehicle model. Theoretically, the increase of τ_{int} will make the actual first-order filter closer to the ideal integrator and the static error will be less. However, in our case the change of the time constant within the range of 10–100 (s) did not make a significant difference on the steady-state errors. Simulations were performed with 0.8 g step load, proportional gain $K_p = 2$, integral gain $K_{\text{int}} = 20$ and varying $\tau_{\text{int}} = 10,\ 50,\ 100$. The relative displacements between the

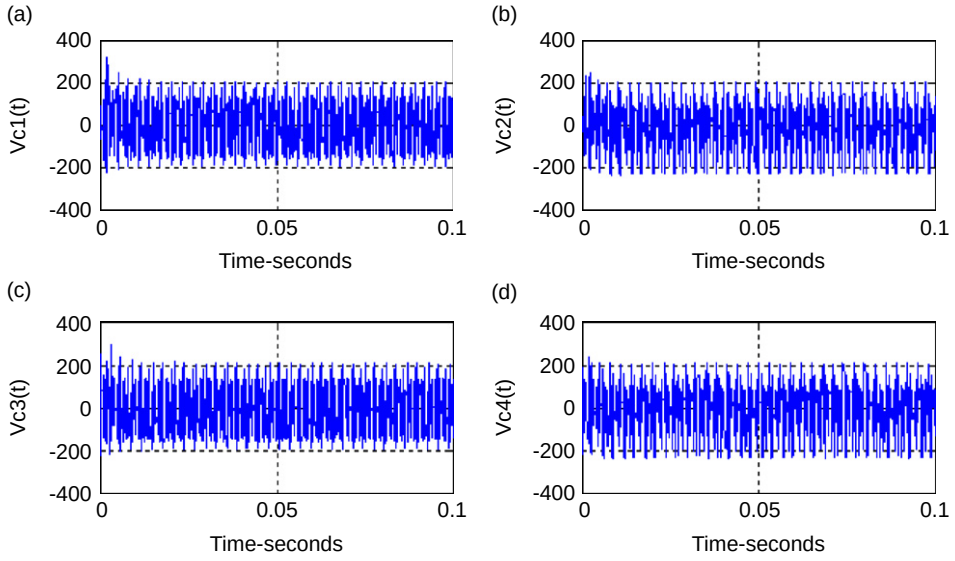

Fig. 13. Coil voltage of magnetic bearings: (a) voltage of coil 1, (b) voltage of coil 2, (c) voltage of coil 3, and (d) voltage of coil 4.

rotor and the stator for the three cases are all equal to 254 μM. The power amplifier coil voltage outputs with the imbalance input $e = 0.635\,\mu\text{M}$ and 23 standard runout harmonics for the three time constants are all equal to 70 V.

In these simulations, the steady-state error of 254 μM is too large for the flywheel system. This means that the magnetic bearing is too "soft" to support the rotor. The proportional gain of the controller adds stiffness to the effective support provided by the magnetic bearings. Theoretically, stability permitting, increasing the integral gain will also bring down the error. Simulations were performed with varying proportional gain and integral gain to examine the relative displacement between the rotor and the stator. When the controller parameters are chosen as $K_p = 8$, $K_{\text{int}} = 80$, and $\tau_{\text{int}} = 50$ subject to a step inertial load 0.8 g in Y direction, the simulation shows that (a) the maximum displacement is 109.2 μM, which occurred at the second magnetic bearing (node 113 vs. node 52); (b) the steady-state displacement is 12.7 μM, which provides desirable control accuracy.

There are two main specifications for the inertial load test: the maximum displacement and the steady-state displacement between the rotor and the stator. The maximum displacement is determined by the controller dynamics: the controller gains and the time constants all affect this specification. The steady-state displacement is determined by the integral term. A non-zero pole is employed in the integrator to avoid the DC instability that would result from a pure integrator. Hence there is a steady-state error. Note that the steady-state outputs of the two radial bearings in the Y direction maintain constant voltages. This is the result of the integrator and is necessary to overcome the steady-state error due to the step load in the Y direction. On the other hand, the control outputs of the two radial bearings in Z channel go to zero as the transient diminishes. The transient output of the controller in the Z direction is caused by the gyroscopic coupling of the spinning rotor.

Simulations were performed for the imbalance and runout test. The power amplifier coil voltage outputs against the imbalance eccentricity and the 23 standard runout harmonics for the three time constants are all equal to 120 V. The increase in the power amplifier coil voltage from 70 to 120 V is due to the increase of the proportional gain from $K_p = 2$ to $K_p = 8$. For comparison, the integral controller was removed while retaining all the remaining control parameters to determine how the integral control affects the inertial load response. The simulations without integrator show that the maximum displacement is 119 μM in the second bearing, larger than that with the integrator. The steady-state displacement in the second bearing increased to 104 μM, much larger than the result of 12.7 μM in the case with integrator. The advantage of including the integrator is well demonstrated by these simulations.

The integral term provides a 90-degree phase lag at DC, which can be considered as negative damping at low frequency. Because of this phase lag property, the integral control may cause instability of the system. Hence it is very important to examine the stability with the proportional-integral-derivative controller over the complete operating range. An iterative process is required in determining the proportional-integral-derivative controller gains, lead compensator zeros and poles, notch-tracking harmonics or fixed center frequencies. The final parameters shown here all result from iterative searches. The eigenvalues showed that the controller with these parameters yields stable response over the complete operating speed range. The recommended values for the proportional-integral-derivative controller derived from the simulations are: $K_p = 8$, $K_d = 0.0008$, $K_{\text{int}} = 80$, and$\tau_{\text{int}} = 50$, utilizing an imbalance eccentricity (e) of $0.635\,\mu\text{M}$ and information on the 23 harmonics in sensor runout data as described earlier.

5. Conclusions

The controller design approach for magnetically supported flywheel systems presented provide a comprehensive and systematic synthesis for high-speed rotordynamic systems with very high-dimensional flexible structural model. The finite element model is employed to study the open-loop rotordynamic behavior and the closed-loop controller development, and provides insights into stability, frequency response, time transient process, and control effectiveness to disturbances. The large number of flexible modes and speed-dependent modes made the controller development particularly challenging. Although the size, speed and construction of the modules presented a challenge for magnetic suspension control, it is concluded that a physical controller can be realized to provide stable rotor suspension with good disturbance rejection, for all planned operating speeds. Control of this high number of flexible modes was achieved to provide stability and disturbance rejection, even when high-speed operation required modes to be traversed by the running speed and harmonic-related forces, and with the rotor position feedback sensors and magnetic bearing stator mounted on the flexible housing.

The control of flexible rotor systems with active magnetic bearings exhibits the following main approaches: First, analysis of rotordynamics of the open-loop systems was conducted. Second, closed-loop mathematical model with structural variables and controller states was constructed and simulated. Finally, the controllers were optimized to provide stable operations over the entire speed ranges of the flywheel. The flywheel system supported by active magnetic bearings has demonstrated the properties of robustness to the standard sensor runout patterns, mass imbalances and inertial load impact. The coil peak voltages were within the specific limits for the selected power amplifiers with adequate margin against clipping, and the peak vibration was suppressed within the catcher bearing gaps for the given runout and imbalance disturbances.

References

[1] M. Dussaux, The industrial applications of active magnetic bearing technology, Proceedings of the Second International Symposium of Magnetic Bearings, Tokyo, Japan, July 1990, pp. 33–38.

[2] C. Kim, A.B. Palazzolo, A. Kascak, R. Beach, Eddy current effects on the design of rotor-magnetic bearing systems, *Transactions of the ASME, Journal of Mechanical Design* 117B (1995) 162–170.

[3] H. Jeong, C. Kim, C. Lee, Modeling and control of cone-shaped active magnetic bearing system, *Proceedings of the International Symposium on Magnetic Bearings*, Vol. 4, Zurich, Switzerland, August 1994, pp. 23–28.

[4] Y. Zhuravlyov, On LQ-control of magnetic bearing, *IEEE Transactions of Control System Technology* 8 (2) (2000) 344–350.

[5] Y. Zhuravlyov, Linear quadratic optimal control of active magnetic bearings for high speed rotor, *Proceedings of International Symposium on Magnetic Bearings*, Vol. 6, Boston, USA, August 1998, pp. 587–596.

[6] F. Losch, C. Gahler, R. Herzog, μ-Synthesis controller design for a 3 MW pump running in AMBs, *Proceedings of the Sixth International Symposium of Magnetic Bearings*, Cambridge, MA, August 1998, pp. 415–428.

[7] M. Hirata, K. Nonami, T. Ohno, Robust control of a magnetic bearing system using constantly scaled H-infinity control, *Proceedings of the Sixth International Symposium of Magnetic Bearings*, Massachusetts Institute of Technology, Cambridge, MA, August 1998, pp. 713–722.

[8] Shuliang Lei, A. Palazzolo, U. Na, A. Kascak, Fuzzy logic control of magnetic bearings for suppression of vibration due to sudden imbalance, *Proceedings of the Fifth International Symposium of Magnetic Suspension Technology*, Santa Barbara, CA, 1999, pp. 459–471.

[9] Shuliang Lei, Alan Palazzolo, U. Na, A. Kascak, Non-linear fuzzy logic control for forced large motions of spinning shafts, *Journal of Sound and Vibration* 235 (3) (2000) 435–449.
[10] J.M. Vance, *Rotordynamics of turbomachinery*, Wiley, New York, 1998.
[11] R. Herzog, B. Philipp, G. Conrad, L. Rene, Unbalance compensation using generalized notch filters in the multivariable feedback of magnetic bearings, *IEEE Transactions of Control Systems Technology* 4 (5) (1996) 580–586.
[12] G. Schweitzer, H. Bleuler, A. Traxler, *Active Magnetic Bearings: Basics, Properties and Applications of Active Magnetic Bearing*, vdf Hochschulverlag AG an der ETH, Zurich, 1994.
[13] R. Siegwart, R. Larsonneur, A. Traxler, Design and performance of a high speed milling spindle in digitally controlled active magnetic bearing, *Proceedings of the Second International Symposium on Magnetic Bearings*, Tokyo, July 1990, pp. 197–204.